

Formation of NH₂CHO and CH₃CHO upon UV photoprocessing of interstellar ice analogs

RAFAEL MARTÍN-DOMÉNECH,¹ KARIN I. ÖBERG,¹ AND MAHESH RAJAPPAN¹

¹*Center for Astrophysics | Harvard & Smithsonian
60 Garden St., Cambridge, MA 02138, USA*

(Received; Revised; Accepted)

Submitted to ApJ

ABSTRACT

Complex organic molecules (COMs) can be produced by energetic processing of interstellar ice mantles accreted on top of dust grains. Two COMs with proposed energetic ice formation pathways are formamide and acetaldehyde. Both have been detected in Solar System comets, and in different circumstellar and interstellar environments. In this work, we study the NH₂CHO and CH₃CHO formation upon UV photoprocessing of CO:NH₃ and CO:CH₄ ice samples. The conversion from NH₂ radicals to NH₂CHO is 2–16 times higher than the conversion from CH₃ radicals to CH₃CHO under the explored experimental conditions, likely because the formation of the latter competes with the formation of larger hydrocarbons. In addition, the conversion of NH₂ into NH₂CHO at 10 K increases with the NH₃ abundance in the ice, and also with the temperature in CO-dominated CO:NH₃ ices. This is consistent with the presence of a small NH₂ and HCO· reorientation barrier for the formation of NH₂CHO, which is overcome with an increase in the ice temperature. The measured NH₂CHO and CH₃CHO formation efficiencies and rates are similar to those found during electron irradiation of the same ice samples under comparable conditions, suggesting that both UV photons and cosmic rays would have similar contributions to the solid-state formation of these species in space. Finally, the measured conversion yields (up to one order of magnitude higher for NH₂CHO) suggest that in circumstellar environments, where the observed NH₂CHO/CH₃CHO abundance ratio is ~ 0.1 , there are likely additional ice and/or gas phase formation pathways for CH₃CHO.

1. INTRODUCTION

Complex (6+ atoms) organic molecules (COMs, Herbst & van Dishoeck 2009) are detected in a wide variety of astrophysical environments spanning different stages of star formation: from prestellar cores in cold, quiescent dense clouds (Marcelino et al. 2007; Bacmann et al. 2012; Cernicharo et al. 2012; Vastel et al. 2014; Jiménez-Serra et al. 2016); to luke-warm envelopes (Öberg et al. 2010a), hot cores and corinos (see, e.g., Cummins et al. 1986; Blake et al. 1987; Cazaux et al. 2003; Bottinelli et al. 2004; Bianchi et al. 2019), and shocked outflow regions associated with protostars (Arce et al. 2008; Codella et al. 2017; Lefloch et al. 2018); and finally in protoplanetary disks around pre-main sequence stars (Öberg et al. 2015; Walsh et al. 2016; Bergner et al. 2018). COMs are also detected in

our own Solar System comets (most recently in comet 67P/Churyumov-Gerasimenko, Goesmann et al. 2015; Altwegg et al. 2015). This suggests that planetesimals may have delivered organic precursors of more complex prebiotic species to the early Earth, perhaps contributing to the formation of life.

The two COMs of interest for this paper are NH₂CHO (formamide) and chemically similar CH₃CHO (acetaldehyde). Both have been detected in comets (Bockelée-Morvan et al. 2000; Crovisier et al. 2004; Biver et al. 2014; Goesmann et al. 2015), as well as in many of the above mentioned interstellar and circumstellar environments (Rubin et al. 1971; Fourikis et al. 1974; Cazaux et al. 2003; Charnley 2004; Bisschop et al. 2007; Bacmann et al. 2012; Cernicharo et al. 2012; Kahane et al. 2013; Vastel et al. 2014; López-Sepulcre et al. 2015; Codella et al. 2015; Coutens et al. 2016; Jiménez-Serra et al. 2016; Codella et al. 2017; Lee et al. 2019). NH₂CHO, along with its isomer methyl isocyanate (CH₃NCO), is the simplest molecule after isocyanic acid (HNCO)

that contains the peptide bond $-(\text{H}-)\text{N}-\text{C}(=\text{O})-$, the molecular bridge that connects amino acids in proteins. Therefore, it has been proposed as a precursor of amino acids and simple proteins (Saladino et al. 2007, 2012; Barone et al. 2015). CH_3CHO could also play an important role in astrobiology (Hjalmarson et al. 2001).

The origin of interstellar NH_2CHO and CH_3CHO is currently unclear (see López-Sepulcre et al. 2019, for a recent review of the NH_2CHO case). In the MAGICKAL three-phase chemical model (Garrod 2013) both molecules mainly form through radical-radical reactions between NH_2 or CH_3 and $\text{HCO}\cdot$ in icy grain mantles. Ice formation pathways was also suggested by observations of abundance patterns in high-mass star forming regions (Bisschop et al. 2007). However, recent observations of low-mass star-forming regions suggest that gas-phase reactions may instead dominate the formation of these species (Codella et al. 2017; Skouteris et al. 2017). Taking a middle road, Quénard et al. (2018) proposed that combination of gas-phase reactions between NH_2 and H_2CO^1 , and solid-state formation on dust grains (either through hydrogenation of HNCO on the grain surfaces, and/or energetic-processing induced radical-radical reactions in the ice mantles) are needed to explain the observed NH_2CHO abundances across the different astrophysical environments.

One key observation constraining the origin of these species is the $\text{NH}_2\text{CHO}/\text{CH}_3\text{CHO}$ abundance ratio, observed to be ~ 0.1 in hot corinos around low-mass protostars (Lee et al. 2019) and in the cold envelope of the low-mass protostar IRAS 16293-2422B (Jaber et al. 2014). To date, only two studies compare the relative NH_2CHO and CH_3CHO formation through ice radical chemistry in comparable ice samples. Jones et al. (2011) and Bennett et al. (2005) experimentally studied the formation mechanism in electron-irradiated $\text{CO}:\text{NH}_3$ and $\text{CO}:\text{CH}_4$ ices, respectively, that could potentially apply to all NH_2CHO and CH_3CHO formation scenarios involving NH_3 and CH_4 molecules. The proposed initial step is the NH_3 N-H or CH_4 C-H bond rupture, producing amino or methyl radicals (NH_2 or CH_3) and $\text{H}\cdot$ radicals with excess energy. The latter react with CO molecules to produce formyl radicals ($\text{HCO}\cdot$) that recombine with neighboring NH_2 or CH_3 to form NH_2CHO and CH_3CHO . They found similar formation rates for both species, so electron or cosmic

¹ This gas-phase reaction was not included in Garrod (2013) because it was thought to have an activation barrier. However, recent works by Barone et al. (2015) and Skouteris et al. (2017) support this formation pathway, which is also needed to explain the observed NH_2CHO abundances in Codella et al. (2017).

ray processing of ices cannot easily explain the observed $\text{NH}_2\text{CHO}/\text{CH}_3\text{CHO}$ abundance ratio of ~ 0.1 .

In space, ice mantles are also exposed to UV photons, especially in the vicinity of massive stars, the surface layers of protoplanetary disks around pre-main sequence stars, the cavities carved out by outflows during the early stages of star formation, and even deep into prestellar cores, where cosmic rays produce secondary UV fields (Cecchi-Pestellini & Aiello 1992; Shen et al. 2004). In this work, we test whether radical ice chemistry in ices exposed to UV radiation can explain the NH_2CHO and CH_3CHO observations around low-mass protostars. We follow the formation of NH_2CHO and CH_3CHO upon vacuum-ultraviolet (VUV) irradiation of a range of $\text{CO}:\text{NH}_3$ and $\text{CO}:\text{CH}_4$ binary ice mixtures to address: 1) the NH_2CHO and CH_3CHO formation efficiencies upon VUV photoprocessing of binary ice mixtures, and 2) the kinetics of NH_2CHO and CH_3CHO formation, including any barriers that could eventually prevent the reaction $\text{NH}_2/\text{CH}_3 + \text{HCO}\cdot$ to take place in interstellar ice mantles. The experimental simulations are described in Sect. 2. The NH_2CHO and CH_3CHO conversion yields and formation cross-sections are presented in Sect. 3, and discussed in Sect. 4 in terms of the two questions considered above. Finally, the main conclusions are summarized in Sect. 5.

2. EXPERIMENTAL SETUP

The experimental simulations were performed using the SPACE CAT² setup located at the Center for Astrophysics. This setup consists in an ultra-high vacuum chamber evacuated by a Pfeiffer Turbo HiPace 400 pump backed by a DUO 10M rotary vane pump to a base pressure of about 5×10^{-10} Torr at room temperature. The relevant features for this work are described below, while more information on the setup can be found in Lauck et al. (2015).

2.1. Ice sample preparation

The $\text{CO}:\text{NH}_3$ and $\text{CO}:\text{CH}_4$ binary ice mixtures were deposited onto a CsI substrate at a temperature of 11 K, achieved by means of a closed-cycle He cryostat. The temperature was monitored by a LakeShore 335 temperature controller with an estimated accuracy of 2 K and a relative uncertainty of 0.1 K. CO (gas, 99.95% purity, Aldrich) and CH_4 (gas, 99.9%, Aldrich) were pre-mixed in a differentially pumped gas line with a base pressure on the order of 10^{-4} Torr and then introduced in the chamber through a 4.8 mm diameter dosing pipe at 17.8

² Surface Processing Apparatus for Chemical Experimentation to Constrain Astrophysical Theories.

Table 1. Summary of the experiments simulating NH₂CHO formation.

Exp.	Ice comp.	Date	Ratio	Irr. T (K)	Thickness (ML ^a)	N(NH ₂ CHO) ^b (ML ^a)	$\frac{N(\text{NH}_2\text{CHO})^b}{\Delta N(\text{NH}_3)}$ (%)
1	CO:NH ₃	08/2018	1:1.2	-	202 [20]	-	-
2	CO:NH ₃	08/2018	2.0:1	11	176 [18]	4.5 [1.0]	19.2 [4.3]
3	CO:NH ₃	02/2019	2.1:1	10	172 [17]	4.4 [1.0]	14.7 [3.3]
4	CO:NH ₃	08/2018	2.1:1	20	221 [22]	6.6 [1.7]	27.2 [7.1]
5	CO:NH ₃	02/2019	2.1:1	19	208 [21]	5.4 [1.2]	18.2 [4.1]
6	CO:NH ₃	03/2019	2.9:1	19	255 [26]	6.4 [1.6]	27.9 [6.8]
7	CO:NH ₃	09/2018	1.2:1	12	231 [23]	3.7 [0.9]	17.3 [4.0]
8	CO:NH ₃	02/2019	1:1.0	10	179 [18]	9.9 [2.2]	21.1 [4.6]
9	CO:NH ₃	03/2019	1.5:1	10	247 [25]	8.1 [1.8]	20.9 [4.6]
10	CO:NH ₃	03/2019	1.1:1	10	226 [23]	8.5 [1.9]	23.9 [5.2]
11	CO:NH ₃	03/2019	1:1.0	19	191 [19]	10.5 [2.5]	34.9 [8.2]
12	CO:NH ₃	09/2018	1.1:1	24	195 [20]	4.7 [1.0]	36.8 [7.9]
13	CO:NH ₃	02/2019	1:1.1	24	159 [16]	6.1 [1.4]	27.1 [6.3]
14	CO:NH ₃	08/2018	1:2.3	12	203 [20]	7.9 [1.7]	28.4 [6.0]
15	CO:NH ₃	03/2019	1:3.1	10	208 [21]	8.5 [1.9]	34.2 [7.7]
16	CO:NH ₃	03/2019	1:3.2	10	222 [22]	7.9 [1.8]	25.8 [5.9]
17	CO:NH ₃	08/2018	1:3.2	20	198 [20]	7.9 [1.8]	29.1 [6.7]
18	CO:NH ₃	03/2019	1:2.8	19	221 [22]	8.7 [2.0]	33.9 [8.0]
19	CO:NH ₃ :NH ₂ CHO	10/2018	118:149:1	-	281 [28]	-	-
20	NH ₂ CHO	10/2018	-	-	35 [4]	-	-

NOTE— ^a 1 ML = 10¹⁵ molecules cm⁻². Uncertainties include a 20% error due to the use of band strengths from pure ices (see text). ^b After a fluence of 6.5 × 10¹⁷ photons cm⁻².

mm from the substrate. For the CO:NH₃ ice mixtures, CO and NH₃ (gas, 99.99%) were introduced through two different dosing pipes (due to the corrosive nature of NH₃) located at 30.5 mm from the substrate. In each experiment, the total thickness of the deposited ice samples was ~200 ML (1 ML = 10¹⁵ molecules cm⁻²).

We also deposited pure NH₂CHO and CH₃CHO ices, as well as CO:NH₃:NH₂CHO and CO:CH₄:CH₃CHO ternary ice mixtures. These ice samples were not photoprocessed, but used to confirm the assignments of the infrared bands and the desorption temperatures of the two main photoproducts. To that end, we used NH₂CHO (liquid, 99.5% purity, Sigma) and CH₃CHO (liquid, 99.5% purity, Aldrich) without further purification, after applying two freeze-thaw-pump cycles. We note that pure NH₂CHO ice was deposited at 119 K, well above the desorption temperatures of N₂ and CO₂, that appeared as contaminants when depositing NH₂CHO at

11 K³. In any case, the pure NH₂CHO IR spectrum at 119 K shows only subtle differences with respect to the one collected at 11 K.

2.2. VUV photoprocessing of the ice samples

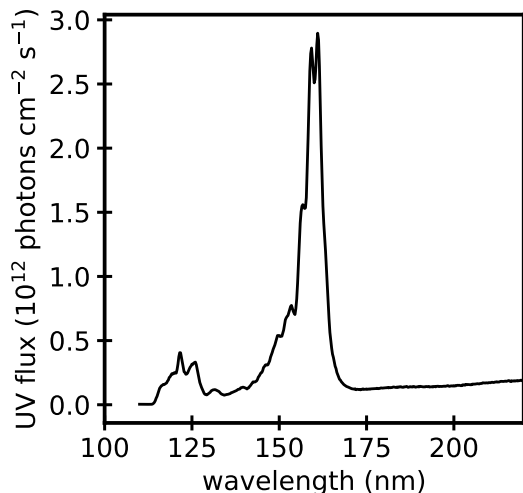
After deposition, the ice samples were VUV irradiated using a deuterium lamp (Hamamatsu H2D2 L11798), either at the deposition temperature (11 K) or at 20 K. The factory lamp emission spectrum in the VUV range (110-220 nm) is presented in Fig. 1, and features a strong emission band at ~160 nm that correspond to the emission of molecular deuterium, and weaker emission (~30% of the flux at 160 nm) around Ly- α wavelengths. The total VUV flux at the sample position,

³ Liquid NH₂CHO was warmed up prior to the deposition to increase its vapor pressure in the gas line, leading to the dissociation of some NH₂CHO molecules. The dissociation products (including N₂ and CO₂) were introduced in the chamber along with the intact NH₂CHO molecules, and could have become incorporated to the ice samples if the substrate temperature was below their desorption temperature.

Table 2. Summary of the experiments simulating CH₃CHO formation.

Exp.	Ice comp.	Date	Ratio	Irr. T (K)	Thickness (ML ^a)	N(CH ₃ CHO) ^b (ML ^a)	$\frac{N(\text{CH}_3\text{CHO})^b}{\Delta N(\text{CH}_4)}$ (%)
21	CO:CH ₄	08/2018	1.4:1	-	131 [13]	-	-
22	CO:CH ₄	05/2018	3.4:1	12	155 [16]	0.50 [0.11]	6.1 [1.4]
23	CO:CH ₄	06/2018	2.6:1	12	200 [20]	0.57 [0.16]	4.6 [1.3]
24	CO:CH ₄	06/2018	4.6:1	20	167 [17]	0.16 [0.04]	2.4 [0.6]
25	CO:CH ₄	05/2018	1.5:1	12	132 [13]	0.43 [0.10]	4.3 [1.0]
26	CO:CH ₄	05/2018	1:1.1	21	110 [10]	0.36 [0.10]	3.2 [0.9]
27	CO:CH ₄	06/2018	1:2.1	11	191 [19]	0.48 [0.10] ^c	2.3 [0.5] ^c
28	CO:CH ₄	08/2018	1:2.4	20	217 [22]	0.39 [0.09]	2.3 [0.5]
29	CO:CH ₄ :CH ₃ CHO	08/2018	9.6:6.8:1	-	116 [12]	-	-
30	CH ₃ CHO	08/2018	-	-	47 [5]	-	-

NOTE—^a 1 ML = 10^{15} molecules cm^{-2} . Uncertainties include a 20% error due to the use of band strengths from pure ices (see text). ^b After a fluence of 6.5×10^{17} photons cm^{-2} . ^c After a fluence of 5.2×10^{17} photons cm^{-2} due to the lack of good IR spectra for higher fluences.

**Figure 1.** Emission spectrum of the Hamamatsu H2D2 L11798 lamp in the VUV range.

measured with a NIST calibrated AXUV-100G photodiode placed in front of the substrate, varied between $3.7\text{--}7.4 \times 10^{13}$ photons $\text{cm}^{-2} \text{s}^{-1}$. Sample irradiation times varied between 210 and 380 min, resulting in total fluences of $6.2\text{--}12.8 \times 10^{17}$ photons cm^{-2} . For comparison, assuming a secondary UV flux of $\sim 10^4$ photons $\text{cm}^{-2} \text{s}^{-1}$ in the interior of dense cores (Shen et al. 2004), interstellar ices are exposed to a fluence of $\sim 3 \times 10^{17}$ photons cm^{-2} during a cloud lifetime of $\sim 10^6$ years.

We ran three series of experimental simulations, two for the CO:NH₃ (08–09/2018 and 02–03/2019), and one for the CO:CH₄ (05–06/2018) ice samples. Some

differences were found in the NH₂CHO formation cross-sections (Sect. 3.3) between experiments of the two series performed under the same conditions, that we think are due to subtle fluctuations in the energy distribution of the VUV photons over time. These fluctuations do not affect the COM formation efficiencies in Sect. 3.2, since they are removed when the COMs formation is normalized to the parent molecules dissociation. Tables 1 and 2 summarize all the experimental simulations presented in this paper, along with the date they were performed. They include the two blank experiments (1 and 21) with no photoprocessing of the binary ice mixtures, used to confirm that NH₂CHO and CH₃CHO were formed upon VUV irradiation of the ice samples.

2.3. IR ice spectroscopy

During the experimental simulations, the ice samples were monitored with a Fourier transform infrared (FTIR) spectrometer (Bruker Vertex 70v with a liquid-nitrogen-cooled MCT detector) in transmittance. Spectra were collected with a normal IR beam incidence after deposition and after photoprocessing of the binary mixtures, and every 5 minutes during warm-up of the photoprocessed ices (see below); and with a 45° incidence every 10 minutes during the photoprocessing of the ice samples; with a resolution of 1 cm^{-1} in the range 4000–400 cm^{-1} , and averaged over 128 interferograms. When necessary, the IR spectra were baseline corrected using a *spline* function with the IDL software. The column density of selected species in the ice was calculated from the IR spectra using the equation

$$N = \frac{1}{A} \int_{band} \tau_\nu d\nu, \quad (1)$$

where N is the column density in molecules cm^{-2} , τ_ν the optical depth of the absorption band (2.3 times the absorbance), and A the band strength in cm molecule^{-1} , and corrected from the 45° IR beam incidence, unless otherwise indicated. For CO, NH_3 , and CH_4 , the integrated optical depth over a particular IR feature was calculated numerically using the function *int_tabulated* in IDL. For NH_2CHO and CH_3CHO , the corresponding IR bands were fitted to a Gaussian using the *curve_fit* function in Python (see Figures 6 and 7). Band strengths are usually measured for pure amorphous ices (Table 3), and the same values are adopted for ice mixtures, which introduces an uncertainty of about 20% in the absolute column densities (d’Hendecourt & Allamandola 1986)⁴ For most of the data analysis we only take into account the statistical errors, however, since the band strength differences between ice experiments of similar composition should be small.

Table 3. IR features used to calculate the column density of selected ice components. Frequencies and band strengths for pure ices at 10–25 K.

Molecule	Frequency (cm^{-1})	Band strength (cm molec^{-1})
CO	2139	1.1×10^{-17} ^a
NH_3	1070	1.7×10^{-17} ^b
CH_4	1304	8.0×10^{-18} ^c
NH_2CHO	1388	6.8×10^{-18} ^d
CH_3CHO	1728	3.0×10^{-17} ^e

NOTE—^aGerakines et al. (1995), ^bSchutte et al. (1996), ^cBouilloud et al. (2015), ^dBrucato et al. (2006), ^eHudson & Ferrante (2020)

2.4. Temperature Programmed Desorption of photoprocessed ice samples

At the end of the photoprocessing, the ice samples were warmed from the irradiation temperature up to 250 K using a 50 ω thermofoil heater with a heating rate of 2 K min^{-1} , until their complete sublimation was achieved. The IR spectra of the samples were collected every 5 min (10 K), and a quadrupole mass spectrometer

⁴ This uncertainty could be higher in very diluted ice mixtures, not used in this work. For example, a factor of 3 difference is found for the CH_4 1304 cm^{-1} IR band strength in a 20:1 CO: CH_4 mixture, compared to the value in a pure amorphous ice (Hudgins et al. 1993)

(QMS; Pfeiffer QMG 220M1) was used to detect the desorbing molecules in the gas phase. The initial ice components, CO, NH_3 , and CH_4 , were monitored through the mass fragments $m/z = 28$ (CO^+), 17 (NH_3^+), and 15 (CH_3^+ , almost the same intensity as the main mass fragment CH_4^+ , shared with atomic oxygen), respectively; and the photoproducts NH_2CHO and CH_3CHO through the mass fragments $m/z = 45$ (NH_2CHO^+), and $m/z = 29$ (HCO^+ , main mass fragment for acetaldehyde), leading to the temperature programmed desorption (TPD) curve for each species.

3. RESULTS

3.1. Fiducial CO: NH_3 and CO: CH_4 VUV irradiation experiments

Our standard experimental simulations to test the formation of NH_2CHO and CH_3CHO upon VUV irradiation of CO: NH_3 and CO: CH_4 ice mixtures, respectively, are 1:1 ice samples irradiated at 10–12 K (Experiments 7–10 for NH_2CHO , and Exp. 25 for CH_3CHO , see Tables 1 and 2).

3.1.1. Formation of NH_2CHO

The top panels of Fig. 2 show the IR spectrum in the 2400–975 cm^{-1} range of the fiducial CO: NH_3 1:1 ice mixture (Exp. 10) before irradiation (black), and after a fluence of 6.5×10^{17} photons cm^{-2} (violet). Photodestruction of CO and NH_3 is observed by the decrease of the C=O stretching band peaking at 2135 cm^{-1} (left panel), and the NH_3 umbrella band at 1060 cm^{-1} (right panel). At the same time, formation of NH_2CHO is evidenced by the growth of IR bands at 1698 cm^{-1} , 1390 cm^{-1} , and 1325 cm^{-1} , which correspond to the position of NH_2CHO IR bands in a CO: NH_3 : NH_2CHO ice mixture (middle panels), and in a pure NH_2CHO ice (bottom panels). Small features due to the formation of CO_2 (2342 cm^{-1}), OCN^- (2160 cm^{-1}), and unreacted HCO^\cdot radicals (1850 cm^{-1}) are also observed. Two IR features peaking at 1561 cm^{-1} and 1496 cm^{-1} remained unassigned.

The top panel of Fig. 3 shows the TPD curve of NH_2CHO ($m/z = 45$) after photoprocessing of the CO: NH_3 ice sample (violet). Thermal desorption of the photoproduced NH_2CHO peaks at a temperature of 197 K, in between the desorption temperature of a pure NH_2CHO ice (207 K, bottom panel) and NH_2CHO in a CO: NH_3 : NH_2CHO ice mixture (189 K, middle panel). Desorption was also observed at the same temperature for the mass fragments $m/z = 44$ (NHCHO^+) and $m/z = 29$ (HCO^+), shown in the Appendix. Since the intensity of the $m/z = 44$ desorption peak is lower than that of the $m/z = 45$ peak, even if some trapped CO_2

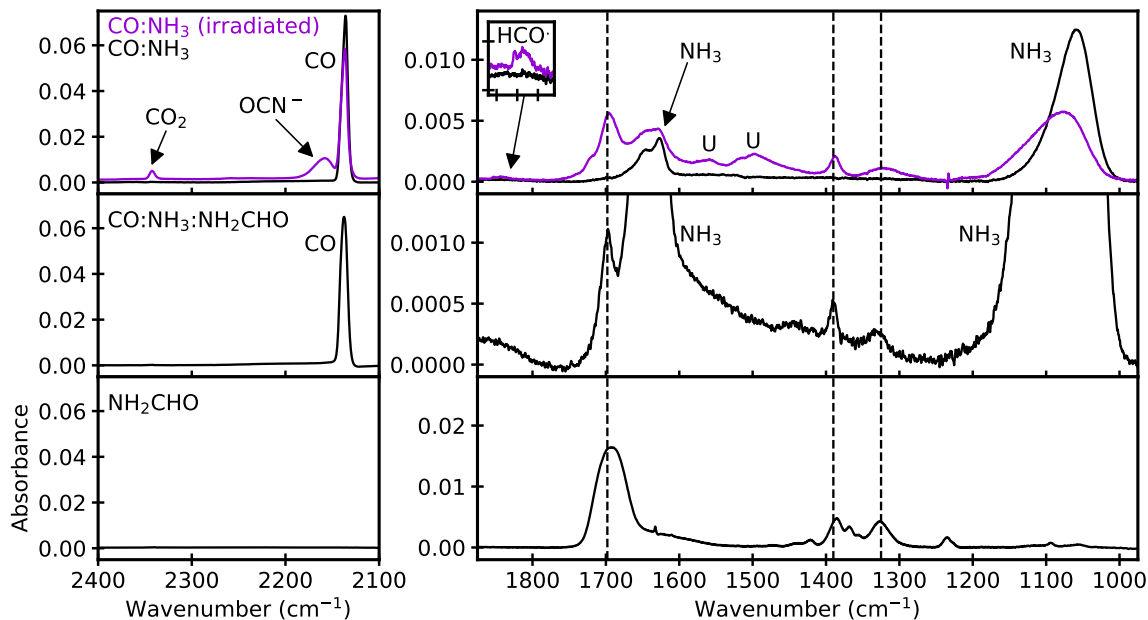


Figure 2. *Top panels:* IR spectrum of a CO:NH₃ 1:1 ice sample before (solid black) and after (solid violet) VUV photoprocessing at 10 K (Exp. 10). *Middle panels:* IR spectrum of a CO:NH₃:NH₂CHO 118:149:1 ice sample at 12 K (Exp. 19). *Bottom panels:* IR spectrum of a pure NH₂CHO ice deposited at 119 K (Exp. 20). IR band assignments are indicated in the panels (U corresponds to unassigned features). Vertical dashed lines indicate the positions of the three most intense NH₂CHO IR bands.

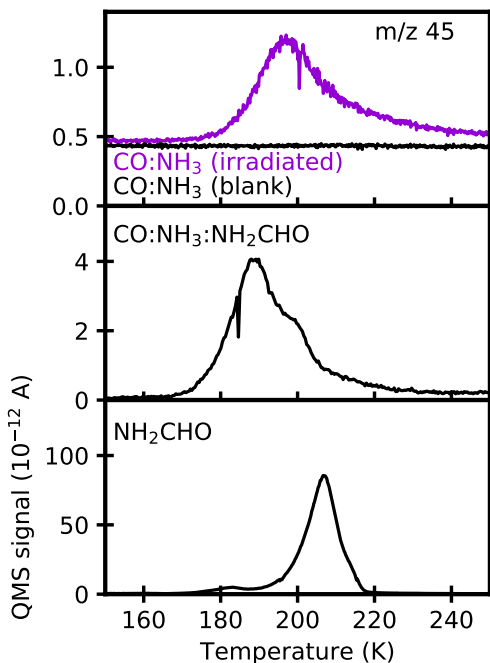


Figure 3. The TPD curve of the $m/z = 45$ fragment corresponding to the produced NH₂CHO after photoprocessing of a CO:NH₃ ice sample (*top panel*, solid violet) is compared to the thermal desorption of NH₂CHO in a CO:NH₃:NH₂CHO ice mixture (*middle panel*), and a pure NH₂CHO ice (*bottom panel*). No NH₂CHO desorption was detected for the blank experiment with no photoprocessing of the CO:NH₃ ice sample (*top panel*, solid black).

molecules are contributing to the former, the potential contribution of ¹³CO₂ molecules to the latter would be negligible. No $m/z = 45$ signal was detected in the blank experiment with no irradiation of the CO:NH₃ ice sample. Similar results were found for the rest of the experiments in Table 1, i.e., NH₂CHO is formed in all irradiated CO:NH₃ ice experiments demonstrating that NH₂CHO formation in cold CO:NH₃ ices is robust.

3.1.2. Formation of CH₃CHO

The top panels of Fig. 4 show the IR spectrum in the 2400–975 cm⁻¹ range of the CO:CH₄ ice mixture in Exp. 25 before irradiation (black) and after a total fluence of 8.8×10^{17} photons cm⁻² (violet). A new IR feature due to the formation of CH₃CHO appears at 1728 cm⁻¹. This feature is slightly blueshifted in mixtures with CO and CH₄ (middle panels) with respect to its position in a pure CH₃CHO ice (bottom panels). The other CH₃CHO IR bands at 1426 cm⁻¹, 1348 cm⁻¹, and 1123 cm⁻¹ could not be unambiguously detected in the photoprocessed ice. IR bands corresponding to the intermediate photoproduct HCO· are observed at 1855 cm⁻¹ and 1092 cm⁻¹, and also the CO₂ feature at 2342 cm⁻¹. The band peaking at 1465 cm⁻¹ corresponds to the -CH₂- scissors and/or the CH₃- antisymmetric deformation vibrational modes in saturated hydrocarbons (C_xH_{2x+2}), that are also produced during irradiation of CO:CH₄ ice mixtures, while the CH₃- symmetric deformation vibrational mode could contribute to the band at

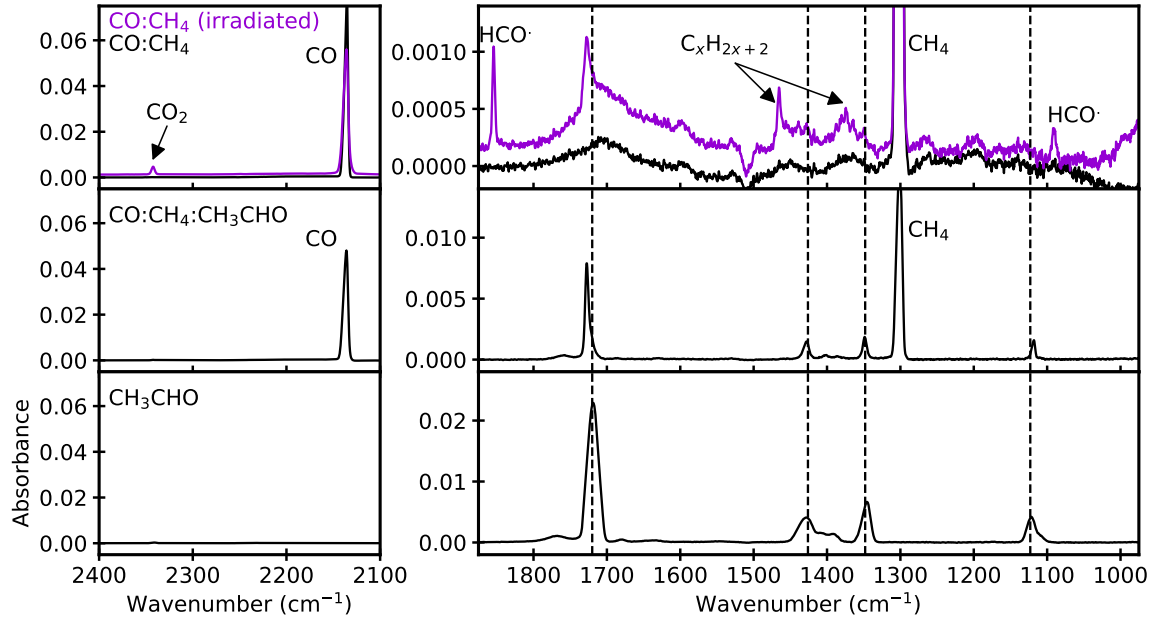


Figure 4. *Top panels:* IR spectrum of a CO:CH₄ ice sample before (solid black) and after (solid violet) VUV photoprocessing (Exp. 25). *Middle panels:* IR spectrum of a CO:CH₄:CH₃CHO 9.6:8.4:1 ice sample at 11 K (Exp. 29). *Bottom panels:* IR spectrum of a pure CH₃CHO ice at 11 K (Exp. 30). IR band assignments are indicated in the panels. Vertical dashed lines indicate the position of the IR features of pure acetaldehyde at 1720 cm⁻¹, 1426 cm⁻¹, and 1348 cm⁻¹.

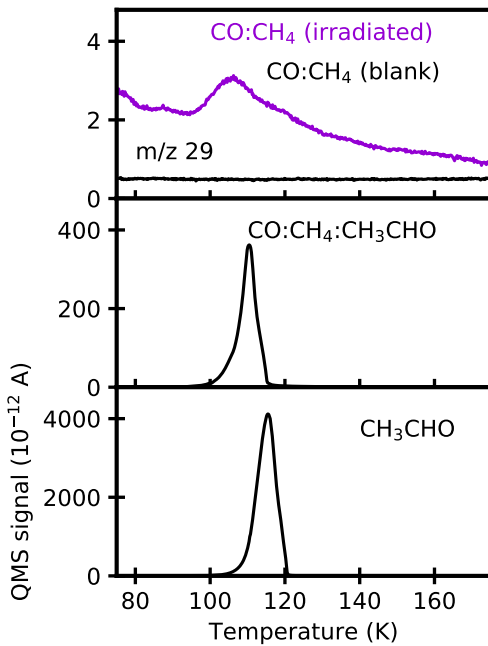


Figure 5. The TPD curve of the $m/z = 29$ (HCO^+) fragment used to verify the CH_3CHO production after photoprocessing of a CO:CH₄ ice sample (*top panel*, solid violet) is compared to the thermal desorption of CH_3CHO in a CO:CH₄:CH₃CHO ice mixture (*middle panel*), and a pure CH₃CHO ice (*bottom panel*). No CH_3CHO desorption was detected for the blank experiment (*top panel*, solid black)

1377 cm⁻¹. For example, additional C₂H₆ IR features are detected at 2972 cm⁻¹ and 2980 cm⁻¹ (not shown in Fig. 4).

The TPD curve of HCO^+ ($m/z = 29$) corresponding to CH_3CHO molecules after photoprocessing of the ice sample in Exp. 24 is presented in Fig. 5. The photo-produced acetaldehyde thermal desorption peaks at 106 K, similar to a pure acetaldehyde ice (115 K, bottom panel), and acetaldehyde in a CO:CH₄ matrix (110 K, middle panel). Desorption was also observed at the same temperature for the mass fragment $m/z = 15$ (CH_3^+ , shown in the Appendix), and tentatively detected for the mass fragments $m/z = 44$ (CH_3CHO^+) and $m/z = 43$ (CH_2CHO^+) (not shown). CO desorption was not detected in this temperature range (see Appendix), ruling out any ¹³CO contribution to the $m/z = 29$ desorption peak. No $m/z = 29$ signal was detected for the blank experiment with no irradiation of the ice mixture. Results were similar for the rest of experiments in Table 2.

3.2. NH₂CHO and CH₃CHO formation efficiencies

To quantify the formation efficiencies of NH₂CHO and CH₃CHO in photoprocessed CO:NH₃ and CO:CH₄ ices, we define the conversion yield as the amount of photodissociated NH₃ or CH₄ that is converted into NH₂CHO and CH₃CHO after a given fluence (we have used 6.5×10^{17} photons cm⁻² unless otherwise indicated). This enables us to remove the effects of VUV

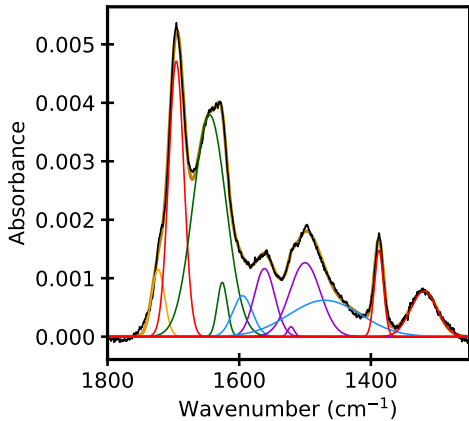


Figure 6. Example fit to assigned and unassigned features in the IR spectrum of a VUV photoprocessed CO:NH₃ ice sample (Exp. 9). The measured IR spectrum is shown in black with the total fit overlaid in gold. Eleven Gaussians were used for the fit (see text), including three corresponding to the NH₂CHO IR features at 1698 cm⁻¹, 1390 cm⁻¹, and 1325 cm⁻¹ (red), one probably corresponding to H₂CO (orange), two corresponding to the NH₃ deformation mode (green), three for the unassigned features (purple), and two extra Gaussians to better reproduce the shape of the spectrum (blue).

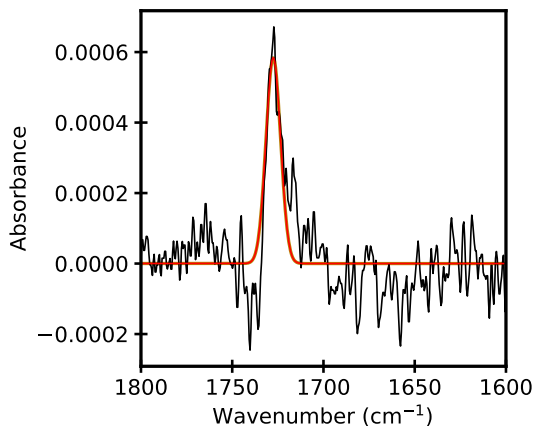


Figure 7. Example fit to the 1728 cm⁻¹ IR feature appeared in the IR spectrum of a CO:CH₄ ice mixture at the end of the irradiation in Exp. 24. The measured IR spectrum is shown in black with the fit in red.

lamp energy distribution fluctuations between experiments, temperature-dependent effective photodissociation rates, as well as the different NH₃ and CH₄ photodissociation cross-sections (Cruz-Díaz et al. 2014a,b), when comparing COM formation in experiments with different ice compositions and irradiation temperatures (see Tables 1 and 2). Assuming that photodissociation (photodesorption can be considered negligible compared to photodissociation in thick ices) of NH₃ and

CH₄ mainly produces NH₂ (as a first approximation, see, e.g., Martín-Doménech et al. 2018, and references therein) and CH₃ (Öberg et al. 2010b)⁵, this conversion yield describes the fraction of photoproduced radicals that react to form NH₂CHO and CH₃CHO compared to other outcomes, i.e. it is effectively a product branching ratio measure.

The NH₃ and CH₄ column densities were estimated from the umbrella IR band at 1060 cm⁻¹, and the CH₄ deformation band at 1304 cm⁻¹, respectively, using Eq. 1. The corresponding band strengths are listed in Table 3, and the integrated absorbances were calculated using the function *int.tabulated* in IDL (Sect. 2.3).

The production of NH₂CHO was estimated from the 1390 cm⁻¹ IR band, since it is the least blended band in our experiments. To isolate the 1390 cm⁻¹ IR band, the IR spectra collected during photoprocessing of the ice samples were fitted in the 1800–1250 cm⁻¹ range with eleven different Gaussians (Fig. 6), including three corresponding to the three NH₂CHO IR features at 1698 cm⁻¹, 1390 cm⁻¹, and 1325 cm⁻¹ (red); two for the doubled-peak NH₃ deformation band at ~1642 cm⁻¹ and ~1626 cm⁻¹ (green); and three Gaussians for the two unassigned bands peaking at ~1561 cm⁻¹ and ~1496 cm⁻¹ (purple). In addition, we used one additional Gaussian for the weak shoulder peaking at ~1722 cm⁻¹ in the NH₂CHO C=O stretching band (1698 cm⁻¹), probably corresponding to H₂CO (orange). One Gaussian centered at ~1593 cm⁻¹, and one broader Gaussian centered at ~1435 cm⁻¹ were also included in the fit to better reproduce the shape of the spectrum (blue). The central position of the Gaussians was one of the free parameters used during the fits, and typically varied within 3 cm⁻¹ with respect to the above positions from one spectrum to another.

The production of CH₃CHO was estimated from the C=O stretching IR band at 1728 cm⁻¹. This band could in theory include a contribution from H₂CO, but since no H₂CO signal was observed during the TPD of the photoprocessed CO:CH₄ ices, we assume that CH₃CHO is the only contributor to the 1728 cm⁻¹ band. This feature was typically weak in our experiments, and the line intensity was extracted using a single Gaussian fit (Fig. 7).

⁵ Since some photodissociation events could lead to the production of CH₂, the conversions presented here should be treated as upper limits. Öberg et al. (2010b) estimated a CH₃:CH₂ branching ratio $\geq 3:1$ for the photoprocessing of a pure CH₄ ice with a microwave-discharged hydrogen-flow lamp peaking at Ly- α , but found that this ratio was even higher in binary mixtures with H₂O.

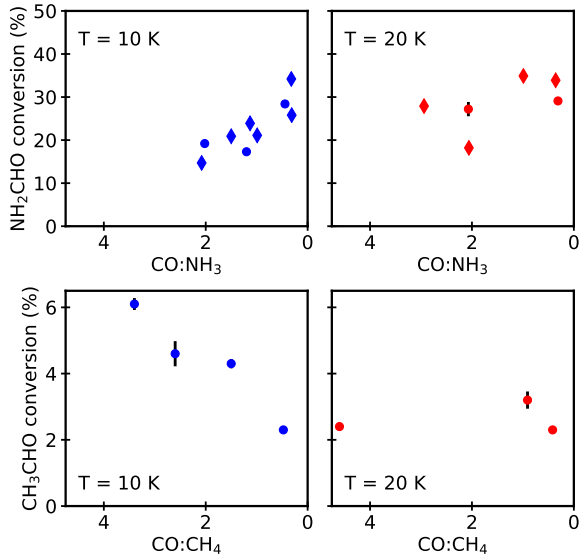


Figure 8. Conversion from NH_2 or CH_3 radicals into NH_2CHO or CH_3CHO after irradiation of $\text{CO}:\text{NH}_3$ or $\text{CO}:\text{CH}_4$ ice mixtures of different compositions (*top* and *bottom* panels, respectively) with 6.5×10^{17} photons cm^{-2} , performed at $T = 10$ K (*left panels*) and $T = 20$ K (*right panels*). The conversion yields are listed in the last column of Tables 1 and 2, and represented by blue and red markers for the experimental simulations performed at $T \sim 10$ K (*left panels*) and $T = 20$ – 24 K (*right panels*), respectively; with error bars in black (without taking into account the 20% uncertainty due to the use of pure ice band strengths in ice mixtures, see Sect. 2.3). We have used dots and diamonds for the first and the second series of $\text{CO}:\text{NH}_3$ experiments, respectively.

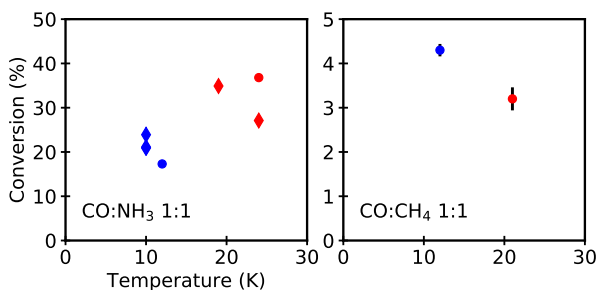


Figure 9. Conversion from NH_2 or CH_3 radicals into NH_2CHO or CH_3CHO after irradiation of 1:1 $\text{CO}:\text{NH}_3$ or $\text{CO}:\text{CH}_4$ ice samples (*left* and *right* panel, respectively) at $T \sim 10$ K (blue markers) and $T = 20$ – 24 K (red markers) with 6.5×10^{17} photons cm^{-2} . Error bars in black do not take into account the 20% uncertainty due to the use of pure ice band strengths in ice mixtures (see Sect. 2.3). We have used dots and diamonds for the first and the second series of $\text{CO}:\text{NH}_3$ experiments, respectively.

The conversion yield after a fluence of 6.5×10^{17} photons cm^{-2} for the fiducial $\text{CO}:\text{NH}_3$ 1:1 ice mixtures photoprocessed at 10 K (Exp. 7-10) is 17-24% (see last column of Table 1), while the conversion yield for the fiducial $\text{CO}:\text{CH}_4$ 1:1 ice mixture VUV irradiated at 12 K (Exp. 25) is $\sim 4\%$ (see last column of Table 2). The conversion from NH_2 to NH_2CHO is, therefore, ~ 6 times higher than the conversion from CH_3 to CH_3CHO under similar experimental conditions.

In addition to our standard experimental simulations, we carried out experiments with different ice compositions and irradiation temperatures to study their influence in the COM formation efficiencies and kinetics. The conversion yields after a fluence of 6.5×10^{17} photons cm^{-2} are presented in the last columns of Tables 1 and 2, and shown in Fig. 8. They range from 15% to 37%, approximately, for the case of NH_2CHO , and 2–6% for CH_3CHO , depending on the ice composition and the irradiation temperature. The conversion from NH_2 to NH_2CHO is up to one order of magnitude higher than the conversion from CH_3 to CH_3CHO under the different experimental conditions explored in this work.

The left top panel in Fig. 8 show that the conversion from NH_2 radicals into NH_2CHO is slightly dependent on the ice composition at low temperatures ($T \sim 10$ K), with higher conversions for the NH_3 -rich ices: an increase in NH_3 concentration by a factor of 6 produces an increase in conversion yield of a factor of 2; whereas no clear trend with the composition is observed when the ice is irradiated at $T \sim 20$ K (upper right panel in Fig. 8). On the other hand, the conversion yield from CH_3 radicals into CH_3CHO *decreases* with CH_4 concentration at $T \sim 10$ K (a factor of ~ 3 variation for a factor of ~ 7 change in the $\text{CO}:\text{CH}_4$ ratio, bottom left panel of Fig. 8), while the CH_3CHO conversion yield seems to be independent of the composition at $T = 20$ K (bottom right panel of Fig. 8).

Regarding the COMs formation at different temperatures, the NH_2CHO conversion yield is observed to increase with temperature, but only in ices with $\text{CO}:\text{NH}_3$ ratio ≥ 1 (top panels in Fig. 8). Conversely, the CH_3CHO formation efficiency decreases with temperature in ices with $\text{CO}:\text{CH}_4$ ratio ≥ 1 . Figure 9 highlights the opposing temperature trends observed for NH_2CHO and CH_3CHO conversion yields.

3.3. NH_2CHO and CH_3CHO formation kinetics

The formation of NH_2CHO and CH_3CHO molecules upon processing of $\text{CO}:\text{NH}_3$ and $\text{CO}:\text{CH}_4$ ices can be parameterized with a pseudo-first order kinetic equation (Jones et al. 2011; Bennett et al. 2005):

Table 4. Summary of the best-fit NH₂CHO formation cross-sections

Exp.	Ratio	Irr. T (K)	$\sigma_{form}(\text{NH}_2\text{CHO})$ ($\times 10^{-18} \text{ cm}^2$)
2	2.0:1	11	3.0 [0.2]
3	2.1:1	10	6.3 [0.2]
4	2.1:1	20	3.5 [0.4]
5	2.1:1	19	4.1 [0.2]
6	2.9:1	19	4.5 [0.2]
7	1.2:1	12	2.1 [0.1]
8	1:1.0	10	4.1 [0.1]
10	1.1:1	10	3.6 [0.1]
11	1:1.0	19	2.5 [0.2]
12	1.1:1	24	2.7 [0.1]
13	1:1.1	24	1.9 [0.1]
14	1:2.3	12	3.8 [0.1]
15	1:3.1	10	3.2 [0.1]
16	1:3.2	10	1.6 [0.1]
17	1:3.2	20	3.9 [0.2]
18	1:2.8	19	4.1 [0.2]

NOTE—Values in brackets correspond only to the fit errors. (The fit did not converge for Exp. 9.)

Table 5. Summary of the best-fit CH₃CHO formation cross-sections.

Exp.	Ratio	Irr. T (K)	$\sigma_{form}(\text{CH}_3\text{CHO})$ ($\times 10^{-18} \text{ cm}^2$)
22	2.7:1	12	3.3 [0.2]
23	2.1:1	12	5.2 [0.4]
24	3.7:1	20	5.1 [0.8]
25	1.2:1	12	4.4 [0.6]
26	1:1.4	21	7.6 [0.7]
27	1:2.6	11	2.2 [0.4]
28	1:3.0	20	9.8 [0.6]

NOTE—Values in brackets correspond only to the fit errors.

$$N = N_{ss} \times (1 - e^{-\sigma_{form} F}) \quad (2)$$

where N_{ss} represents the NH₂CHO or CH₃CHO steady state column densities, σ_{form} is their appar-

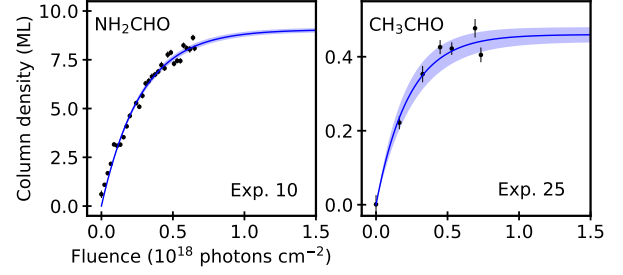


Figure 10. NH₂CHO and CH₃CHO growth curves (*left* and *right* panels, respectively) during photoprocessing of CO:NH₃ (Exp. 10) and CO:CH₄ (Exp. 25) ices (black dots), along with the best-fit kinetic model (blue) and the 1σ confidence region for the fit (shadowed zone) (best-fit formation cross-sections are listed in Tables 4 and 5). Column densities are calculated from the spectra taken with an angle of 45° with respect to the infrared beam during irradiation of the ice samples (see Sect. 2.3).

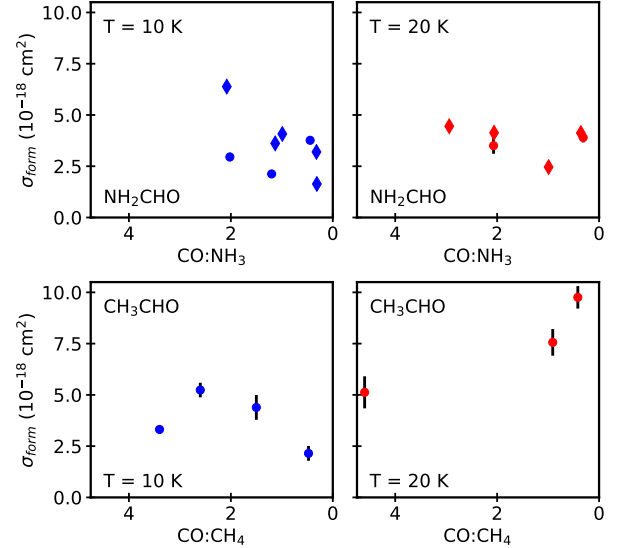


Figure 11. NH₂CHO and CH₃CHO formation cross-sections upon VUV irradiation of CO:NH₃ and CO:CH₄ ice mixtures (*top* and *bottom* panels, respectively). The cross-section values are listed in Tables 4 and 5, and represented by blue and red markers for the experimental simulations performed at $T \sim 10 \text{ K}$ (*left* panels) and $\sim 20 \text{ K}$ (*right* panels), respectively; with error bars in black. We have used dots and diamonds for the first and the second series of CO:NH₃ experiments, respectively.

ent formation cross-section in cm^2 , and F the incident fluence in photons cm^{-2} . Fig. 10 presents the NH₂CHO and CH₃CHO growth curves (product column densities versus fluence) for the fiducial CO:NH₃ and CO:CH₄ 1:1 ice mixtures photoprocessed at 10 K (Exp. 10 and 25), along with the best-fit kinetic models. The NH₂CHO and CH₃CHO formation cross-sections are (3.6 ± 0.1)

$\times 10^{18} \text{ cm}^{-2}$ and $(4.4 \pm 0.6) \times 10^{18} \text{ cm}^{-2}$, respectively (see last columns of Tables 4 and 5). Within experimental uncertainties (note that experimental errors are larger than the fit errors), the formation kinetics of both COMs are similar under the same experimental conditions. Therefore, the higher NH_2CHO conversion yield at a given fluence (Sect. 3.2) is not due to a faster formation of NH_2CHO compared to CH_3CHO .

The NH_2CHO and CH_3CHO growth curves in experiments 2–18 and 22–28 are presented in the Appendix along with the best-fit kinetic models. The NH_2CHO and CH_3CHO formation cross-sections are listed in Tables 4 and 5, and shown in Fig. 11. They range from $2 \times 10^{18} \text{ cm}^{-2}$ to $6 \times 10^{18} \text{ cm}^{-2}$, approximately, in the case of NH_2CHO , and $3 \times 10^{18} - 10 \times 10^{18} \text{ cm}^{-2}$ for CH_3CHO , depending on the ice composition and irradiation temperature. The bottom line is that the formation kinetics of these COMs are always of the same order under all the experimental conditions explored in this work. We do not identify any consistent and significant trend for the COM formation cross-sections with the ice composition or irradiation temperature.

We note that at 10 K we derive different cross sections by up to a factor of 3 in the two NH_2CHO formation experimental series. The inferred substantial experiment-to-experiment variation may mask small temperature or composition dependencies on the formation cross sections. We speculate that this is due to subtle fluctuations of the VUV lamp emission spectrum with time (Sect. 2), which demonstrates the limits inherent with studying photoprocesses with broadband lamps. It also points to the presence of non-thermal processes at 10 K that strongly depend on the specific photon energy. No difference across experimental series is seen for the 20 K experiments, or when considering formation efficiencies.

4. DISCUSSION

4.1. COM formation mechanisms

In Sect. 3.2 we show that the conversion yield from NH_2 to NH_2CHO is up to one order of magnitude higher than the conversion yield from CH_3 to CH_3CHO under similar experimental conditions. At the same time, the measured conversion yields follow opposite trends: while the NH_2CHO conversion yield increases with the NH_3 abundance and the irradiation temperature, the CH_3CHO conversion yield decreases with both the CH_4 abundance and the irradiation temperature. This suggests that even though the formation pathway is expected to be the same for both species (Jones et al. 2011; Bennett et al. 2005), their formation processes present some peculiarities that lead to the observed differences.

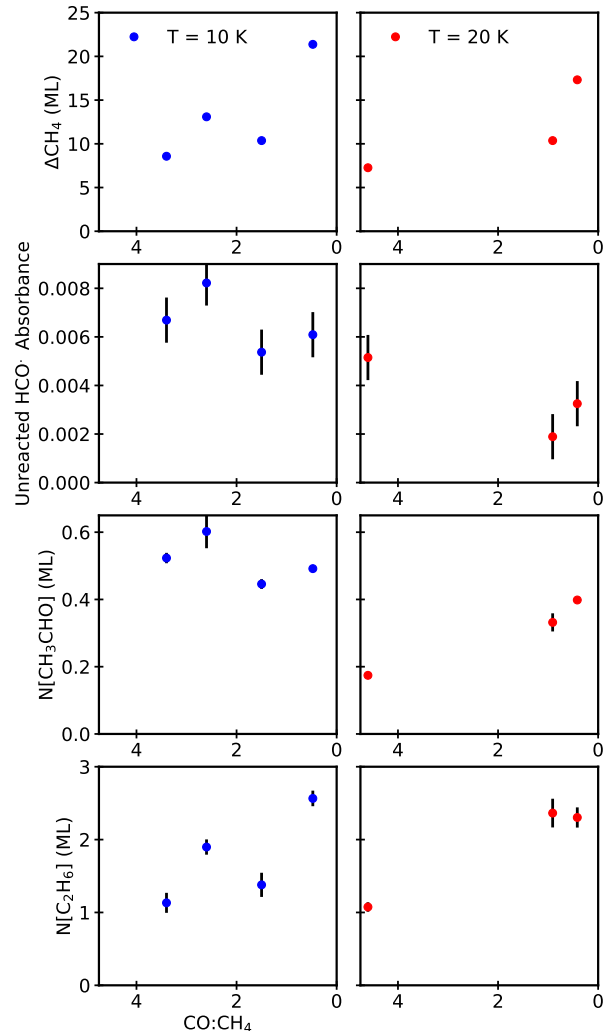


Figure 12. From top to bottom, number of photodestroyed CH_4 molecules; IR absorbance corresponding to the unreacted HCO radicals; and column density of the photoproduced CH_3CHO and C_2H_6 (based on the 1465 cm^{-1} IR band, and using the band strength for CH_4 -rich ices extracted from Molpeceres et al. 2016), after photoprocessing of $\text{CO}:\text{CH}_4$ ice samples at 10 K (left) and 20 K (right).

The main question that needs to be addressed is the much higher NH_2CHO conversion yield compared to the CH_3CHO yield. The NH_2CHO and CH_3CHO formation cross-sections are roughly similar (normalized to the steady state abundances, see Sect. 3.3) and cannot account for the order of magnitude difference in the conversion yields. A possible explanation is that there are more efficient processes that compete with the formation of CH_3CHO during the processing of $\text{CO}:\text{CH}_4$ ices, compared to the processes competing with the formation of NH_2CHO molecules in $\text{CO}:\text{NH}_3$ ices. One of these competing processes is the recombination of CH_3

radicals to form larger saturated hydrocarbons⁶ such as C_2H_6 . These are indeed detected in the IR spectra of the photoprocessed CO:CH₄ ices (Fig. 4). On the other hand, N_2H_4 is not detected after photoprocessing of the CO:NH₃ ice samples. This implies that the recombination of CH₃ radicals is probably more efficient than the recombination of NH₂ radicals, relatively to the formation of CH₃CHO and NH₂CHO.

The efficient recombination of CH₃ radicals to form larger hydrocarbons (along with the inefficient recombination of NH₂ to form N_2H_4) could also explain some of the trends observed for the CH₃CHO and NH₂CHO conversion yields. Upon photoprocessing of CO:CH₄ ices of any composition at 10 K, a similar number of CH₃CHO molecules is produced in every experiment (~ 0.5 ML, Fig. 12), while the number of produced CH₃ radicals increases with the CH₄ ice abundance (see the increasing CH₄ photodissociation in the top left panel of Fig. 12). The number of unreacted HCO \cdot radicals in these experiments is roughly constant (Fig. 12), so decreased HCO \cdot production with increased CH₄ abundance cannot explain the decrease in the CH₃CHO conversion yield with CH₄ ice abundance. On the other hand, the number of produced C_2H_6 molecules (based on the 1465 cm^{-1} IR band shown in Fig. 4) follows the same trend observed for the number of photodestroyed CH₄ molecules, leading to a constant conversion yield of $\sim 13\%$ ⁷, ~ 2 – 5 times higher than the CH₃CHO conversion yield. These trends can be understood if CH₃ radicals prefer to react with one another rather than with HCO \cdot radicals when given the option, and considering that diffusion of radicals is not efficient at low temperatures in the absence of non-thermal, hot-atom diffusion, so only neighboring radicals can react at 10 K. Under these premises, CH₃ and HCO \cdot radicals would need to form next to each other to form a CH₃CHO molecule, without any additional CH₃ radical that would result in the formation of C_2H_6 . This is more likely to happen in CO-rich ices rather than in CH₄-rich ices, explaining the observed trend in the CH₃CHO conversion yield at 10 K.

At higher temperatures, radicals are expected to become mobile (see, e.g., Garrod 2019) and non-neighboring CH₃ radicals may also react with one another forming C_2H_6 molecules. The number of produced CH₃CHO molecules thus decrease down to ~ 0.2 ML in

CO-rich ices (see Table 2 and Fig. 12). This supports the hypothesis that CH₃ radicals preferentially react with one another instead that with HCO \cdot radicals. However, the corresponding increase in the hydrocarbon production at 20 K compared to the production at 10 K is low, on the order of the C_2H_6 column density errors shown in the bottom panels of Fig. 12.

To explain the increase of the NH₂CHO conversion yield with the NH₃ ice abundance when the ice samples are irradiated at 10 K, we speculate that the HCO \cdot and NH₂ radicals need a particular orientation for their reaction to proceed and produce NH₂CHO, and that this particular orientation is more likely to take place in NH₃-rich ices. Whether this is true also for the CH₃ + HCO \cdot reaction is difficult to say with the present data, and we therefore focus on the NH₂ + HCO \cdot reaction.

While some HCO \cdot radicals remained unreacted after irradiation of the 2:1 and 1:1 CO:NH₃ ice samples at 10 K (left and middle upper panels of Fig. 13), no HCO \cdot radicals were detected after irradiation of the NH₃-rich ice samples (right upper panel of Fig. 13). At the same time, an increase in the NH₂CHO conversion yield is observed. Therefore, all HCO \cdot radicals formed in NH₃-rich ices are able to react with NH₂ radicals and form NH₂CHO. A possible explanation to this is that the CO:NH₃ ratio decrease in the ice samples is accompanied by an increase of the NH₂:HCO \cdot ratio during photoprocessing of the ice samples. In that case, a particular HCO \cdot radical can be potentially surrounded by a larger number of NH₂ radicals. This would increase the probability that at least one of them is oriented in such way that enables the recombination of the two radicals and the formation of NH₂CHO⁸. The HCO \cdot IR feature detected after photoprocessing of 2:1 and 1:1 CO:NH₃ ices at 10 K decreases its intensity when the photoprocessed ice samples are warmed to temperatures above 20 K (left and middle upper panels of Fig. 13), and is not detected at $T \sim 40$ K. At these temperatures, radicals become mobile, and the remaining HCO \cdot could overcome this small reorientation barrier and find properly oriented NH₂ radicals. This leads to an increase of ~ 30 – 40% in the NH₂CHO column density (left and middle bottom panels inf Fig. 13), that increases the conversion yield to similar values as those found for NH₃-rich ices. We note that unreacted HCO \cdot radicals are not detected

⁶ We note that simple hydrocarbons are usually detected in protostellar and circumstellar environments (see, e.g., Öberg et al. 2008; Pontoppidan et al. 2014; Guzmán et al. 2015).

⁷ Since it takes two CH₃ radicals to form one C_2H_6 molecule, this means that $\sim 26\%$ of the produced CH₃ radicals recombine to form C_2H_6 in any experiment.

⁸ We note that, according to the reaction mechanism explained in Sect. 1, it is not possible to form a larger number of HCO \cdot than NH₂ radicals, while it is possible to produce a larger number of NH₂ than HCO \cdot radicals. Therefore, the opposite situation (i.e., a NH₂ radical surrounded by a large number of HCO \cdot radicals) is much less probable in CO-rich ices.

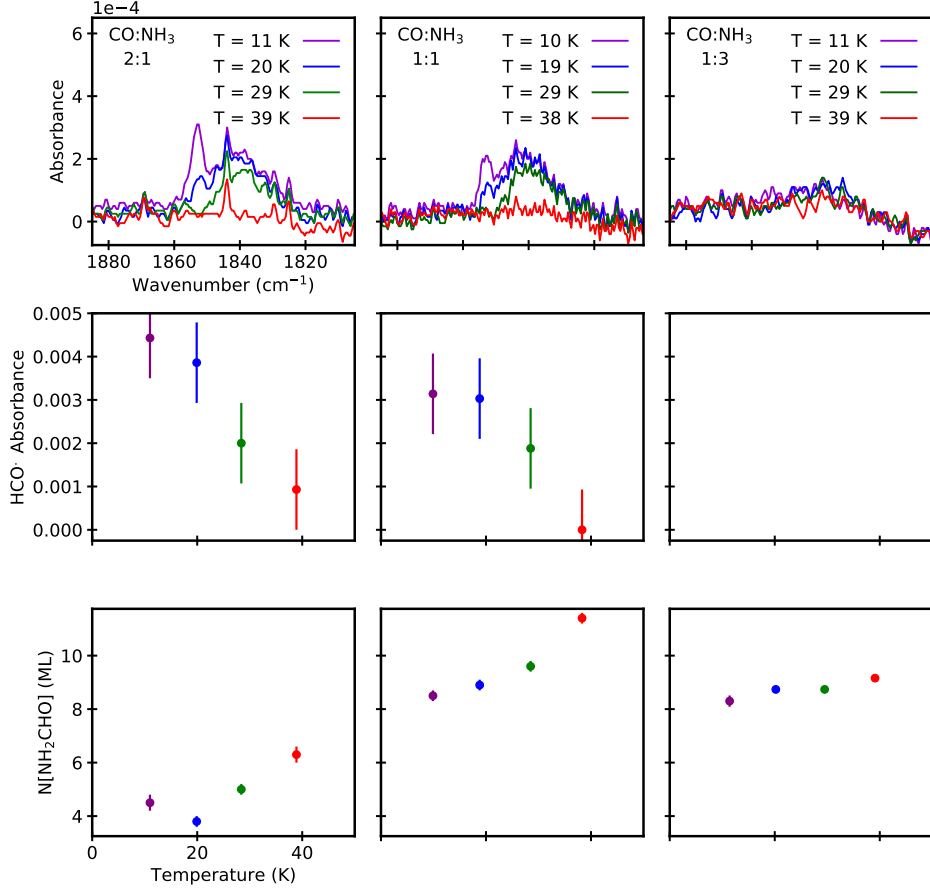


Figure 13. The HCO \cdot IR feature detected after photoprocessing of 2:1 (Exp. 2) and 1:1 (Exp. 10) CO:NH $_3$ ices at T = 10 K (*left and middle upper panels*) decreases its intensity at T > 20 K (*left and middle middle panels*, the HCO \cdot column density was not calculated to the lack of an experimental band strength value in the literature)

, due to the increased radical mobility that leads to an increase in the NH $_2$ CHO column density (*left and middle bottom panels*). HCO \cdot radicals are not detected in NH $_3$ -rich ices (e.g., Exp. 14, *right panels*).

when CO:NH $_3$ ice samples of any composition are irradiated at 20 K. Therefore, NH $_2$ and HCO \cdot radicals produced at 20 K must be mobile enough to react, regardless of the ice composition. This should result in a flat NH $_2$ CHO conversion yield at 20 K. Unfortunately the conversion yield values measured for our 20 K experiments (upper left panel of Fig. 8) had too much scatter to test this prediction, but we note that they appear to be compatible with a lack of dependence on NH $_3$ concentration. At the same time, the large scatter in the estimation of the formation cross sections at different temperatures (top panels of Fig. 11) prevents us from quantifying this small reorientation barrier.

As stated above, the preferential recombination of CH $_3$ radicals to form larger hydrocarbons during photoprocessing of CO:CH $_4$ ices does not allow us to check whether the radical orientation also plays a role in the formation of CH $_3$ CHO molecules, but we note that the relative orientation of the HCO \cdot and CH $_3$ radicals is supposed to be important for the production of CH $_3$ CHO

in water-rich ices, according to Enrique-Romero et al. (2016).

4.2. Comparison with previous experiments

A number of different NH $_2$ CHO and CH $_3$ CHO solid-state formation pathways have been previously explored experimentally. In the laboratory, hydrogenation chemistry for the formation of NH $_2$ CHO has had mixed results. Hydrogenation of HNCO was proven to be inefficient (Noble et al. 2015), but simultaneous hydrogenation of solid NO and H $_2$ CO, and experiments that combine hydrogenation and UV irradiation of NO in a CO-rich ice analog result in small amounts of NH $_2$ CHO production (Dulieu et al. 2019; Fedoseev et al. 2016).

By contrast, it appears relatively easy to form both NH $_2$ CHO and CH $_3$ CHO upon photon or electron processing of different ices composed of common interstellar ice species. Warm-up of photoprocessed ice mixtures containing H $_2$ O, CH $_3$ OH, CO, and NH $_3$ (Bernstein et al. 1995), UV and soft X-ray irradiation of a

H₂O:CO:NH₃ ice analog (van Broekhuizen et al. 2004; Ciaravella et al. 2019, respectively), UV and electron irradiation of ices containing H₂O, CH₃OH, and NH₃ at 5 and 70 K (Henderson & Gudipati 2015), UV and electron irradiation of a binary CH₃OH:NH₃ ice mixture at 8–10 K (Muñoz Caro et al. 2014; Jheeta et al. 2013, respectively), electron irradiation of a CO:NH₃ ice mixture at 12 K (Jones et al. 2011), all produce detectable amounts of NH₂CHO, among other products. Formation of CH₃CHO is observed during UV irradiation of pure CH₃OH ices (Öberg et al. 2009) and H₂O:CH₄ ice mixtures (Öberg et al. 2010b), and electron irradiation of a CO:CH₄ binary ice mixture at 10 K (Bennett et al. 2005).

4.2.1. Formation efficiencies upon UV processing of different ice samples

We can compare the formation efficiencies at a particular UV fluence of those experiments mentioned above that report such values to those measured in our experiments at similar fluences, to obtain initial constraints on the relative formation efficiencies in different ice environments.

After photoprocessing of the CO:CH₄ ice samples with a fluence of 3.2×10^{17} photons cm⁻², the CH₃CHO percent yield (i.e., the number of CH₃CHO molecules formed with respect to the initial amount of parent CH₄ molecules) ranges from 0.2% to 0.9%, i.e., 0.2–0.9% of the initial CH₄ is transformed into CH₃CHO for the range of ice compositions and irradiation temperatures explored in this work. This is on the same order of the CH₃OH and CH₄ transformed into CH₃CHO after $\sim 3 \times 10^{17}$ photons cm⁻² VUV irradiation of a pure CH₃OH ice and a H₂O:CH₄ ice mixture ($\sim 0.5\%$, Öberg et al. 2009, 2010b, respectively).

On the other hand, the NH₂CHO conversion yield after a fluence of 6.5×10^{17} photons cm⁻² ranges from 15% to 37% (Sect. 3.2), i.e., 3–8% of the initial NH₃ is transformed into NH₂CHO in our experimental simulations. This is one order of magnitude higher than the value measured during warm-up of a photolyzed H₂O:CH₃OH:CO:NH₃ ice sample (<1%, Bernstein et al. 1995) for a fluence 500 times higher. Assuming that the reaction mechanism is the same in both experiments (since both include CO and NH₃ molecules), and that both experiments are close to the steady state (see Fig. 15), then the NH₂ to NH₂CHO conversion yield is decreased in the presence of a water-ice matrix. Therefore, the values presented in this work should be taken with caution, and this decrease should be taken into account when trying to extrapolate these results to the real astrophysical scenario.

4.2.2. Comparison between UV- and electron-processed ices

At the same time, we can compare the percent yields and formation rates upon VUV irradiation of CO:NH₃ and CO:CH₄ ice samples with those reported for the electron irradiation of the same ices in Jones et al. (2011) and Bennett et al. (2005), since the deposited energies and energy fluxes are comparable.

In Jones et al. (2011) and Bennett et al. (2005), the energy deposited after 30–60 minutes of electron irradiation of the ice samples is $1.4\text{--}2.8 \times 10^{18}$ eV cm⁻². In our experiments, a 3.2×10^{17} photons cm⁻² photon fluence experienced by the ice samples correspond to a deposited energy of $\sim 2.5 \times 10^{18}$ eV cm⁻², assuming an average lamp photon energy of ~ 7.75 eV (~ 160 nm, Fig. 1). The NH₂CHO percent yield with respect to the initial amount of NH₃ measured at that fluence ranges from 2% to 6% under the different ice compositions and irradiation temperatures, which are comparable to the 1–2% transformation after 2.8×10^{18} eV cm⁻² dosed upon electron bombardment of CO:NH₃ ices in Jones et al. (2011). The CH₃CHO percent yield with respect to the initial amount of CH₄ was not reported, though, in Bennett et al. (2005).

The $1.4\text{--}2.8 \times 10^{18}$ eV cm⁻² deposited energy on a time span of 30–60 minutes correspond to an energy flux of 7.7×10^{14} eV cm⁻² s⁻¹ during the electron irradiation of the ice samples in Jones et al. (2011) and Bennett et al. (2005). The reported NH₂CHO and CH₃CHO formation rates are $\sim 5 \times 10^{-4}$ s⁻¹, which result in formation cross-sections of $\sim 6.5 \times 10^{-19}$ cm⁻² per incident eV. The formation cross-sections presented in Tables 4 and 5 range from 2 to 5×10^{-18} cm⁻² per incident photon under most of the experimental conditions explored in this work, which correspond to $2.6\text{--}6.5 \times 10^{-19}$ cm⁻² per incident eV, assuming the average lamp photon energy of ~ 7.75 eV, i.e., on the same order than the formation cross-sections found upon electron bombardment of the same ice samples.

4.3. Astrophysical implications

In dense clouds, cosmic rays induce both a secondary UV field by their interaction with the gas-phase H₂ molecules (Cecchi-Pestellini & Aiello 1992; Shen et al. 2004), and secondary keV electrons when interacting with ice molecules (Hovington et al. 1997). The energy dose experienced by the ice mantles from the cosmic-ray induced secondary UV field is thought to be similar in value to the energy contribution from the incoming cosmic rays (Moore et al. 2001). Therefore, since the ice formation efficiencies and timescales of NH₂CHO and CH₃CHO upon both kinds of energetic processing are similar (see above), the contribution of the photopro-

duced NH_2CHO and CH_3CHO in interstellar ices should be comparable to the cosmic-ray induced production.

As stated in the introduction, the observed NH_2CHO -to- CH_3CHO abundance ratio may help us constrain the origin of these species. In our experimental simulations, the conversion yield from NH_2 to NH_2CHO is up to one order of magnitude higher than the conversion yield from CH_3 to CH_3CHO (Sect. 3.2) upon VUV photoprocessing of $\text{CO}:\text{NH}_3$ and $\text{CO}:\text{CH}_4$ ice samples, respectively. Formation of CH_3CHO in ice mantles seems to be quenched by the competing formation of larger hydrocarbons, compared to the formation of NH_2CHO molecules. We expect a similar $\text{NH}_2\text{CHO}:\text{CH}_3\text{CHO}$ ratio for the production of these COMs in interstellar ice mantles, since the results found in this work should be applicable to all ices where NH_2 , CH_3 , and HCO radicals were generated (Sect. 1), and the observed ice abundances of NH_3 and CH_4 with respect to solid H_2O are similar (Boogert et al. 2015). If we assume that interstellar ices are completely desorbed in hot corinos around low-mass protostars, so that the difference in the NH_2CHO and CH_3CHO desorption temperatures does not affect the subsequent gas-phase abundances, we would then expect an order of magnitude higher abundances for NH_2CHO compared to CH_3CHO in such regions, opposite to what is observed (~ 0.1 $\text{NH}_2\text{CHO}/\text{CH}_3\text{CHO}$ abundance ratio, Lee et al. 2019). This suggests that there are additional CH_3CHO formation pathways contributing to the CH_3CHO formation in addition to $\text{CH}_3 + \text{HCO}$ chemistry in both the water-rich ice mantles (e.g., CH_3OH ice processing), and in the gas-phase. NH_2CHO may on the other hand originate from energetic ice processing; more observational constraints are needed to differentiate between this and competing pathways.

5. CONCLUSIONS

1. NH_2CHO and CH_3CHO are formed upon VUV photoprocessing of $\text{CO}:\text{NH}_3$ and $\text{CO}:\text{CH}_4$ ice mix-

tures, respectively. The conversion from radicals to COMs is 2–16 times higher for NH_2CHO compared to CH_3CHO . This is likely due to the competing formation of saturated hydrocarbons that prevents the reaction of CH_3 and HCO radicals to form CH_3CHO .

2. The observed trends in the NH_2CHO conversion yield with the ice composition and the irradiation temperature are compatible with the proposal in Enrique-Romero et al. (2016) that a particular orientation of the radicals (NH_2 and HCO in this case) is needed for the formation of NH_2CHO , with a small reorientation barrier that can be overcome with the temperature. The preferential formation of larger hydrocarbons prevents us from determining whether there is a similar barrier for the formation of CH_3CHO .
3. The formation efficiencies and rates for NH_2CHO and CH_3CHO upon VUV photoprocessing of $\text{CO}:\text{NH}_3$ and $\text{CO}:\text{CH}_4$ ice samples are similar to those found upon electron bombardment of the same ice mixtures for similar deposited energies. We thus expect a comparable contribution from UV photons and cosmic rays for the formation of these species through the radical combination pathways in interstellar ices.
4. Given the measured relative conversion yields for NH_2CHO and CH_3CHO , a significant contribution of other ice- or gas-phase CH_3CHO formation pathways are needed to explain the observed $\text{NH}_2\text{CHO}/\text{CH}_3\text{CHO}$ ratio in hot corinos (~ 0.1).

This work was supported by an award from the Simons Foundation (SCOL # 321183, KO).

APPENDIX

Fig. 14 shows the TPD curves of the main mass fragments corresponding to NH_2CHO (left panel) and CH_3CHO (right panel) after photoprocessing of a $\text{CO}:\text{NH}_3$ and a $\text{CO}:\text{CH}_4$ ice sample, respectively.

The NH_2CHO and CH_3CHO growth curves for the experiments in Tables 1 and 2 are presented in Figures 15, and 16.

REFERENCES

- Altwegg, K., Balsiger, H., Bar-Nun, A., et al. 2015, *Science*, 347, 6220, id.1261952
- Arce, H. G., Santiago-García, J., Jorgensen, J. K., Tafalla, M., & Bachiller, R. 2008, *ApJ*, 681, L21

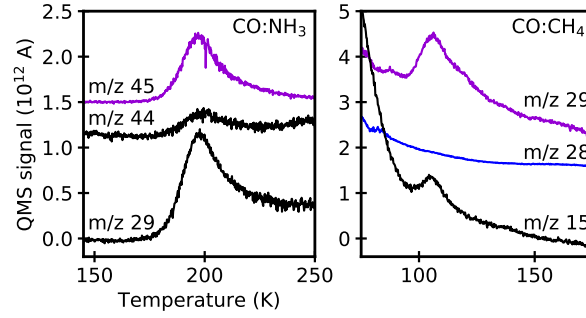


Figure 14. TPD curves of the main mass fragments (violet) corresponding to the produced NH_2CHO (*left panel*) and CH_3CHO (*right panel*), and the following most intense fragments (black) after photoprocessing of a $\text{CO}:\text{NH}_3$ and a $\text{CO}:\text{CH}_4$ ice sample, respectively (see Figures 3 and 5). The $m/z = 28$ mass fragment corresponding to CO is also shown in blue in the right panel.

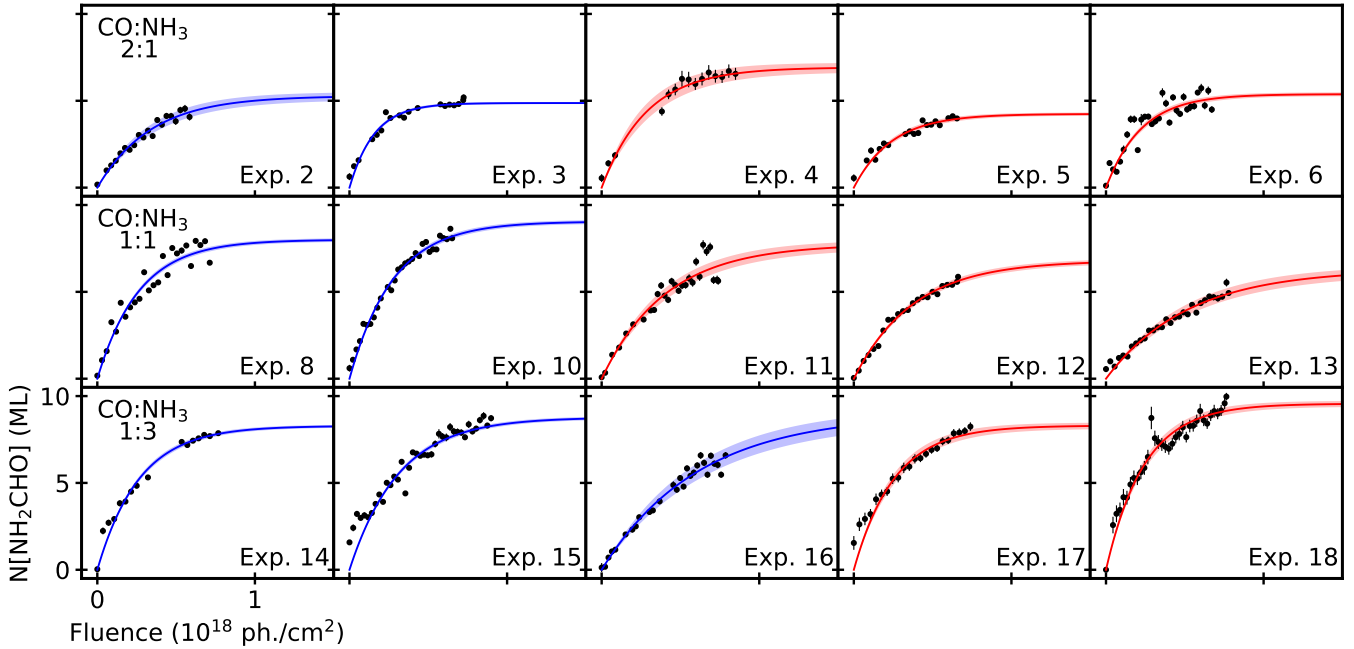


Figure 15. NH_2CHO growth curves during photoprocessing of $\text{CO}:\text{NH}_3$ ices in Exp. 2–18 (black dots), along with the best-fit pseudo-first order kinetic model (blue and red curves for the ~ 10 K and ≥ 20 K ice photoprocessing experiments, respectively) and the 1σ confidence region for the fit (shaded zone). The best-fit parameters and 1σ fit errors are listed in Table 4. Column densities are calculated from the spectra taken with an angle of 45° with respect to the infrared beam during photoprocessing of the ice samples (see Sect. 2.3). Exp. 7 and 9 are not shown for an easier visualization of the experiments performed with similar ice compositions but different irradiation temperatures.

Bacmann, A., Taquet, V., Faure, A., Kahane, C., & Ceccarelli, C. 2012, *A&A*, 541, L12

Barone, V., Latouche, C., Skouteris, D., et al. 2015, *MNRAS*, 453, L31

Blake, G. A., Sutton, E. C., Masson, C. R., & Phillips, T. G. 1987, *ApJ*, 315, 621

Bennett, C. J., Jamieson, C. S., Osamura, Y., & Kaiser, R. I. 2005, *ApJ*, 624, 1097

Bergner, J. B., Guzmán, V.G., Öberg, K. I., Loomis, R., & Pegues, J. 2018, *ApJ*, 857, 1, id69

Bernstein, M.P., Sandford, S.A., Allamandola, L.J., Chang, S., & Scharberg, M.A. 1995, *ApJ*, 454, 327

Bianchi, E., Codella, C., Ceccarelli, C., et al. 2019, *MNRAS*, 483, 2, 1850

Bisschop, S.E., Jorgensen J.K., van Dishoeck, E.F., & de Wachter, E.B.M. 2007, *A&A*, 465, 913

Biver, N., Bockelée-Morvan, D., Dbout, V., et al. 2014, *A&A*, 566, L5

Bockelée-Morvan, D., Lis, D.C., Wink, J.E., et al. 2000, *A&A*, 353, 1101

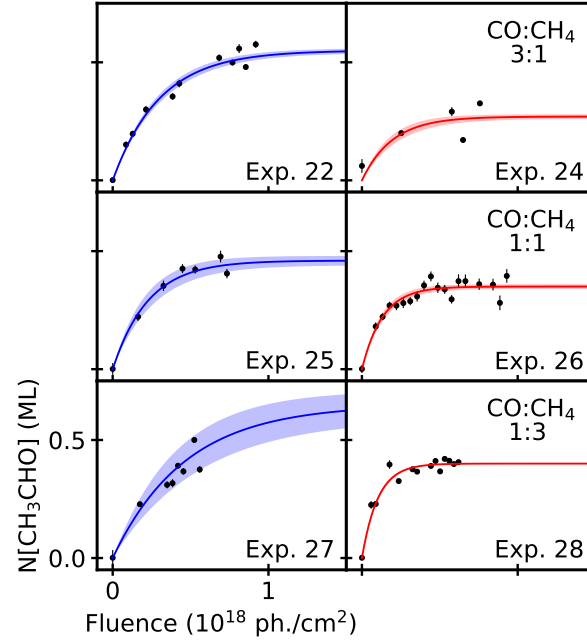


Figure 16. CH_3CHO growth curves during photoprocessing of $\text{CO}:\text{CH}_4$ ices in Exp. 22–28 (black dots), along with the best-fit first order kinetic model (blue and red curves for the ~ 10 K and ~ 20 K ice photoprocessing experiments, respectively) and the 1σ confidence region for the fit (shadowed zone). The best-fit formation cross-sections and 1σ fit errors are listed in Table 5. Column densities are calculated from the spectra taken with an angle of 45° with respect to the infrared beam during photoprocessing of the ice samples (see Sect. 2.3). Exp. 22 is not shown for an easier visualization of the experiments performed with similar ice compositions but different irradiation temperatures.

Boogert, A. C. A., Gerakines, P. A., & Whittet D. C. B. 2015, *ARA&A*, 53, 541
 Bottinelli, S., Ceccarelli, C., Lefloch, B., Williams, J. P., Castets, A., et al. 2004, *ApJ*, 615, 354
 Bouilloud, M. Fray, N., Bénilan, Y., et al. 2015, *MNRAS*, 451, 2145
 Brucato, J.R., Baratta, G.A., & Strazzulla, G. 2006, *A&A*, 455, 395
 Cazaux, S., Tielens, A. G. G. M., Ceccarelli, C., Castets, A., Wakelam, V., et al. 2003, *ApJ*, 593, L51
 Cecchi-Pestellini, C., & Aiello, S. 1992, *MNRAS*, 258, 125
 Cernicharo, J., Marcelino, N., Roueff, E. et al. 2012, *ApJL*, 759, L43
 Charnley, S.B. 2004 *Adv. Space Res.*, 33, 23
 Ciaravella, A., Jiménez-Escobar, A., Cecchi-Pestellini, C., et al. 2019, *ApJ*, 879, 1, id.21
 Codella, C., Ceccarelli, C., Caselli, P., et al. 2017, *A&A*, 605, L3
 Codella, C., Fontani, F., Ceccarelli, C., et al. 2015, *MNRAS*, 449, L11
 Coutens, A., Jorgensen, J.K., van der Wiel, M.H.D., et al. 2016, *A&A*, 590, L6
 Crovisier, J., Bockelée-Morvan, D., Colom, P., Biver, N., & Despois, D. 2004, *A&A*, 418, 1141

Cruz-Díaz, G. A., Muñoz Caro, G. M., Chen, Y.-J., & Yih, T.-S. 2014, *A&A*, 562, A119
 Cruz-Díaz, G. A., Muñoz Caro, G. M., Chen, Y.-J., & Yih, T.-S. 2014, *A&A*, 562, A120
 Cummins, S. E., Linke, R. A., & Thaddeus, P. 1986, *ApJS*, 60, 819
 d’Hendecourt, L. B., & Allamandola L. J. 1986, *A&AS*, 64, 453
 Dulieu, F., Nguyen, T., Congiu, E., Baouche, S., & Taquet, V. 2019, *MNRAS*, 484, L119
 Enrique-Romero, J., Rimola, A., Ceccarelli, . & Balucani, N. 2016, *MNRAS*, 459, 1, L6
 Fedoseev, F., Chuang, K.-J., van Dishoeck, E.F., Ioppolo, S., & Linnartz, H. 2016, *MNRAS*, 460, 4297
 Fourikis, N., Sinclair, M.W., Robinson, B.J., Godfrey, P.D., & Brown, R.D. 1974, *Australian J. Phys.*, 27, 425
 Garrod, R.T., & Herbst, E. 2006, *A&A*, 457, 927
 Garrod, R.T., Weaver, S.L.W., & Herbst, E. 2008, *ApJ*, 682, 283
 Garrod, R.T. 2013, *ApJ*, 765, 60
 Garrod, R.T. 2019, *ApJ*, 884, 1, id.69
 Gerakines, P.A., Moore, M.H., & Hudson, R.L. 2004, *ICARUS*, 170, 202
 Gerakines, P.A., Schutte, W.A., Greenberg, J.M., & van Dishoeck, E.F. 1995, *A&A*, 296, 810

- Gibb, E.L., Whittet, D.C.B., Boogert, A.C.A., & Thielens, A.G.G.M. 2004, *ApJ*, 545, 309
- Goesmann, F., Rosenbauer, H., Bredehöft, J. H., et al. 2015, *Science*, 346, 6247, id.0689
- Gredel, R., Lepp, S., Dalgarno, A., & Herbst, E. 1989, *ApJ*, 347, 289
- Guzmán, V.V., Pety, J., Goicoechea, J.R., et al. 2015, *ApJL*, 800, L33
- Henderson, B.L., & Gudipati, M.S. 2015, *ApJ*, 800, 66
- Herbst, E., & van Dishoeck, E.F. 2009, *Annu. Rev. Astron. Astrophys.*, 47, 427
- Hjalmarson, A., Bergman, P., & Nummelin, A. 2001, in *Proc. 1st European Workshop on Exo-/astro-biology*, ed. P. Ehrenfreund, O. Angerer, & B. Battrick (ESA SP-496; Noordwijk: ESA)
- Hovington, P., Drouin, D., & Gauvin, R. 1997, *Scanning*, 19, 1
- Hudgins, D.M., Sandford, S.A., Allamandola, L.J., & Tielens, A.G.G.M. 1993, *ApJS*, 86, 713
- Hudson, R.L. & Ferrante, R.F. 2020, *MNRAS*, 492, 1, 283
- Jaber, A.A., Ceccarelli, C., Kahane, C., & Caux, E. 2014, *ApJ*, 791, 29
- Jheeta, S., Domaracka, A., Ptasińska, S., Sivaraman, B., & Mason, N.J. 2013, *Chem. Phys. Lett.*, 556, 359
- Jiménez-Serra, I., Vasyunin, A.I., Caselli, P., et al. 2016, *ApJ*, 830, 1, L6
- Jones, B. M., Bennett, C. J., & Kaiser, R. 2011, *ApJ*, 734, 78
- Kahane, C., Ceccarelli, C., Faure, A., & Caux, E. 2013, *ApJ*, 763, L38
- Lamberts, T., Markmeyer, M.N., Kolb, F.J., & Kästner, J. 2019, *ACS Earth and Space Chemistry*, *accepted*
- Lauck, T., Karssemeijer, L., Shulenberg, K., et al. 2015, *ApJ*, 801, 118
- Lee, C-F., Codella, C., Li, Z.-Y., & Liu, S.-Y. 2019, *ApJ*, *accepted*
- Lefloch, B., Bachiller, R., Ceccarelli, C., et al. 2018, *MNRAS*, 477, 4792
- López-Sepulcre, A., Balucani, N., Ceccarelli, C., et al. 2019, *submitted*
- López-Sepulcre, A., Jaber, A.A., Mendoza, E., et al. 2015, *MNRAS*, 449, 2438
- Marcelino, N., Cernicharo, J., Agúndez, M. et al. 2007, *ApJ*, 665, L127
- Martín-Doménech, R., Cruz-Díaz, G.A., & Muñoz Caro, G.M. 2018, *MNRAS*, 473, 2575
- Molpeceres, G., Satorre, M.A., Ortigoso, J., et al. 2016, *ApJ*, 825, 156
- Moore, M.H., Hudson, R.L., & Gerakines, P.A. 2001, *Spectrochimica Acta Part A*, 57, 843
- Muñoz Caro, G.M., Dartois, E., Boduch, P., et al. 2014, *A&A*, 566, A93
- Noble, J.A., Theule, P. Aouididi, H., et al. 2015, *A&A*, 576, A91
- Öberg, K. I., Boogert, A.C.A., Pontoppidan, K.M., et al. 2008, *ApJ*, 678, 1032
- Öberg, K. I., Bottinelli, S., Jorgensen, J. K., & van Dishoeck, E. F. 2010, *ApJ*, 716, 825
- Öberg, K. I., Garrod, R.T., van Dishoeck, E.F., & Linnartz, H. 2009, *A&A*, 504, 3, 891
- Öberg, K. I., van Dishoeck, E.F., Linnartz, H., & Andersson, S. 2010, *ApJ*, 718, 2, 832
- Öberg, K. I., Guzmán, V. V., Furuya, K., et al. 2015, *Nature*, 520, 198
- Pontoppidan, K.M., Salyk, C., Bergin, E.A., et al. 2014, *Protostars and Planets VI*, 363
- Quénard, D., Jiménez-Serra, I., Viti, S., Holdship, J., & Coutens, A. 2018, *MNRAS*, 474, 2796
- Rubin, R.H., Swenson Jr., G.W., Benson, R.C., Tigelaar, H.L., Flygare, W.H., 1971, *ApJL*, 416, 165
- Saladino, R., Botta, G., Pino, S., & Di Lauro, E. 2012 *Chem. Soc. Rev.*, 41, 5526
- Saladino, R., Crestini, C., Ciciriello, F., Costanzo, G., & Di Mauro, E. 2007, *Chem. Biodiversity*, 4, 694
- Schutte, W. A., Gerakines, P. A., Geballe, T. R., van Dishoeck, E. F., & Greenberg, J. M. 1996, *A&A*, 309, 633
- Shen, C. J., Greenberg, J. M., Schutte, W. A., & van Dishoeck, E. F., 2004, *A&A*, 415, 203
- Skouteris, D., Vazart, F., Ceccarelli, C., et al. 2017, *MNRAS*, 468, L1
- van Broekhuizen, F. A., Keane, J. V., & Schutte, W. A. 2004, *A&A*, 415, 425
- Vastel, C., Ceccarelli, C., Lefloch, B., & Bachiller, R. 2014, *ApJL*, 759, L2
- Walsh, C., Loomis, R., Öberg, K., et al. 2016, *ApJ*, 823, L10